

Effects of Thermal Undercooling and Thermal Cycles on the Grain and Microstructure Evolution of TC17 Titanium Alloy Repaired by Wire Arc Additive Manufacturing

Yimin Zhuo

Harbin Institute of Technology

Chunli Yang

Harbin Institute of Technology

Chenglei Fan (✉ 1192018111@qq.com)

Harbin Institute of Technology

Sanbao Lin

Harbin Institute of Technology

Research Article

Keywords: Thermal cycles, Wire arc additive manufacturing, Titanium alloy, Repair, Pulse arc

Posted Date: July 19th, 2021

DOI: <https://doi.org/10.21203/rs.3.rs-665268/v1>

License:   This work is licensed under a Creative Commons Attribution 4.0 International License.

[Read Full License](#)

Version of Record: A version of this preprint was published at The International Journal of Advanced Manufacturing Technology on January 15th, 2022. See the published version at <https://doi.org/10.1007/s00170-021-08445-w>.

Abstract

Wire arc additive manufacturing (WAAM) can be used to repair blades or blisk made of titanium alloy with the advantage of high efficiency and low-cost. In this work, the finite element model of repairing the blade based on the arc heat source was established to investigate it. Results showed that the maximum effect of thermal undercooling appears when the peak current transforms to the base current (1Hz or 5Hz), which will promote the grains refinement with the combination of sufficient constitutional supercooling. Compared to the single-layer deposition, the microstructure in the near-heat affected zone (near-HAZ) of multi-layer deposition changes from the metastable β phases to the extremely fine α phases, which was caused by the repeated thermal cycles.

Introduction

The development process of aero-engine is mainly the improvement process of thrust-weight ratio [1]. Aero-engine blades are the core component of aero-engine. To reduce the weight of blades, designers use the blisk which leaving out the tenon and mortice to replace the traditional blades. However, the blisk are frequently subjected to kinds of damages due to the poor work condition, which results in a serious decrease in engine operating efficiency [2–4]. The replacement of damaged blades is extremely expensive. Therefore, the research of repairing blisk is necessary and will bring huge economic benefit.

For different types of damages, the corresponding repairing methods are different. For the damaged blade with surface cracks, conventional brazing [5, 6] and wide gap braze [7–9] are recommended. These methods have the advantages of no jiggling, no pressure required, and batch processability. Ye et al. [9] successfully repaired the tapered slots defects artificially fabricated in IN738LC superalloy by diffusion brazing with a Ni-Cr-Co-Al-Ta-B filler alloy at 1150°C and then heat treatment was employed. For the fractured blades, linear friction welding [10–12] can achieve the replacement of the whole damaged blade within the damaged blisk instead of discarding it. Meanwhile, additive manufacturing has received a lot of attention in recent years, which has much advantage to repair the damage type of partial defects. According to the different of heat sources, AM technology can be divided into three categories: laser additive manufacturing (LAM) [13–15], electron beam additive manufacturing (EBAM) [16–18], wire arc additive manufacturing (WAAM) [19, 20]. LAM has the advantage of low heat input and high forming accuracy. Zhao et al. [15] repaired wrought Ti17 titanium alloy with small surface defects by LAM technology with powder feeding, and the tensile fracture of repaired specimen occurred in the repaired zone with a mixed dimple and cleavage mode. In the study by Wanjara et al [18], an “extensively eroded” fan blade leading edge was repaired by the wire-feed electron beam additive manufacturing technology. For WAAM technology, it has the unique advantage of low cost and high deposition efficiency (up to 10kg/h) [21].

According to our previous study [22], the feasibility of repairing the damaged blade by the WAAM technology was verified. Meanwhile, the columnar grains can be transformed to equiaxed grains by the combination of pulsed arc and boron addition in our previous work [23]. However, the temperature cycle

feature of the multi-layer repairing deposition based on the arc heat source needs to be further studied. In this work, the finite element model of repairing the blade based on the arc heat source was established. The corresponding relationship of the single-layer and multi-layer deposition between the temperature cycle and the microstructure was investigated. Meanwhile, the user subroutine was developed to investigate the effect of pulsed arc on the grain evolution. The triggering condition and effect position of thermal undercooling was also discussed in detail.

Experimental Procedures And Model

2.1 Experimental setup

As shown in Fig. 1, The WAAM equipment used for repairing TC17 titanium alloy consists of a gas tungsten arc welding (GTAW) torch equipped with a wire feed unit, a trailing shield, and CNC controlled table. The filler material was TC11 titanium alloy wire with a diameter of 1.2 mm, and the base metal was a TC17 titanium alloy plate with the size of 100mm in length, 10mm in width, and 40mm in height. The single-layer deposition was employed with the welding parameters of 100A in welding current, 3mm/s in welding speed, 15mm/s in wire speed. The multi-layer position in our previous work [22] was cited here to explain the relationship of the thermal cycle and microstructure. Meanwhile, the parameters of deposition fabricated by pulsed arc were same as our previous work [23]. This work mainly focused on the simulation computation, which promotes the understanding of grain and microstructure evolution.

2.2 characterization

After the repairing deposition, the metallographic samples were prepared by the standard mechanical polishing method and then etched by the corrosive liquid of HF: HNO₃: H₂O with a volume ratio of 1: 6: 7. The macrostructures were observed by an OLYMPUS-SZX21 optical microscope (OM), and the microstructure was analyzed by a Quanta 200FEG scanning electron microscope (SEM).

2.3 model

The finite element software package, MSC. Marc was used to investigate the grain and microstructure evolution of titanium alloy fabricated by the WAAM technology. The thermophysical properties of TC11 and TC17 were calculated by JMatPro software. The geometry of the single-layer was measured from the experiments separately, and the three-dimensional thermal model and finite element mesh of the single-layer and multi-layer deposition are shown in Fig. 2. Linear brick elements with 8 nodes were used for the thermal simulation. To save the calculation time, dense meshes were used for the deposition, and the meshes became coarser in the -z direction away from the fusion line.

Element birth technique was used to simulate the material deposition procedure [24]. All elements of the deposited block were deactivated at the initial step, and the meshes were activated in turn in successive steps to simulate the deposition process. The user subroutine in the Fortran code was developed to simulate the effect of pulsed arc on the thermal cycle. Meanwhile, the double ellipsoidal heat source [25, 26] was used in this study. All the modeling parameters were identical to the experimental conditions,

including the dimension of the models, welding speed, the cooling time between subsequent layers, etc. The values of convection coefficient and radiation coefficient were determined by running a series of numerical trials based on the experiments. Meanwhile, the thermocouple was attached on the surface of the base metal to record the temperature during the deposition process.

Results And Discussion

3.1 the thermal cycles feature of the sing-layer deposition fabricated by the pulsed arc.

As shown in Fig. 3, the measured curve and the simulated curve of sing-layer deposition fabricated by direct current (DC) agrees well, which indicates the accuracy of the calculation model. Therefore, the calculation parameters of peak and base current of pulsed arc were chosen based on the direct current model. The thermal cycle at the same extracted position of the direct arc model of 1Hz and 5Hz is shown in Fig. 4. The overall trend of the pulsed arc has little different from that of current arc. However, the peak temperature of pulsed arc (1Hz or 5Hz) at the measured point is higher than that of DC arc. It might be caused by the expansion of peak arc, which promotes the heat flux conducting to the measured point. Meanwhile, it is worth noting that there appears an inflection point in the thermal curve of 1Hz pulsed arc, which was caused by the thermal undercooling effect of pulsed arc. Due to the relatively long distance between the arc center and the measured point, the inflection of temperature under the 5Hz pulsed arc is not obvious.

As shown in Fig. 5 and Fig. 6, the thermal cycle at different depositions during one pulsed period of 1Hz and 5Hz was presented. The values of thermal undercooling at the different positions are different. The maximum values of thermal undercooling appears at the position of the peak current transforming to the base current whatever the frequency is 1Hz or 5Hz. As shown in the grain morphology within Fig. 5 and Fig. 6, with the combination of the constitutional supercooling [23], the fine equiaxed grains at the position with the large value of thermal undercooling were formed. It is worth noting that the fine equiaxed grains can be only formed at the position calculated by the center of arc minus the distance between the arc center and the margin of the welding pool when the peak current transforms to the base current. Fine equiaxed grains were hard to be formed at other positions. Since this numerical model only considers the temperature field (without the influence of molten flow), this model can only describe the process of thermal undercooling from a qualitative perspective. This calculation model is helpful to understanding the thermal undercooling and the effecting position of pulsed arc, which promotes the application of pulsed arc on the repairing technology of the damaged blisk.

3.2 Effect of thermal cycle on the microstructure evolution of titanium alloy fabricated by the WAAM technology.

As shown in Fig. 7, horizontal and parallel heat affected bands (HABands) was formed in the deposition layer, which was also observed in other AM process of titanium alloy [27–29]. The position of the HABands is different from that of the fusion line, which indicates the HABands was not formed by the effect of the fusion line, but repeated thermal cycles. The microstructure and corresponding thermal cycle of different positions are shown in Fig. 7(b,c,d). The microstructure between the adjacent HABands is the typical lamellar microstructure with thin and long α phases. The HABands were caused by the coarse and grown α phase (Fig. 7(c)). According to the thermal cycles extracted at corresponding positions, the dwell time of thermal cycles with the peak temperature above the β transus temperature between the HABands and other positions is different. The phase transformation process of α phases to β phases happens when the temperature range is about 600–977°C calculated by JMatPro software (Fig. 8). Therefore, the increased dwell time at this temperature range promotes the growth of α phases, which causes the most coarse α phases with the most dwell time.

3.3 Effect of thermal cycle on the microstructure evolution of titanium alloy fabricated by the WAAM technology.

The heat affected zone (HAZ) has a significant influence on the mechanical properties of the repairing component. Therefore, it is necessary to investigate the microstructure evolution in this zone. As shown in Fig. 9, the microstructure and corresponding thermal cycles at different positions of the HAZ are presented. The microstructure of base metal is a typical basketweave microstructure with the cross distribution of α phase. At the far-HAZ (Fig. 9(c)), the secondary α phase (α_s) within the basketweave microstructure dissolved due to the peak temperature of thermal cycle exceeding the β transus temperature, as shown in Fig. 9(c1). With the position closing to the interface, the peak temperature of thermal cycle increased, as shown in Fig. 9(e1). The relatively longer dwell time caused more dissolution of α_s , and primary α phases (α_p) started to dissolve (Fig. 9(d,e)).

TC17 titanium alloy is one type of rich β stable element titanium alloy, which promotes β phase retained at room temperature [30]. At the near-HAZ, metastable β phases were retained due to the fast cooling rate, the higher peak temperature and more longer dwell time above the β transus temperature, which caused α phases to dissolve completely, as shown in Fig. 9(f). Meanwhile, thin and long α phases distributed crisscross within the sing-layer deposition, which was the base of the microstructure evolution of the multi-layer deposition.

Compare to the sing-layer deposition, the microstructure of the near-HAZ in the multi-layer deposition has the obvious difference, and other positions of the HAZ have little difference. As shown in Fig. 10(b), numbers of acicular α phases formed in the near-HAZ in the multi-layer deposition, which was different from the metastable β phases in the sing-layer deposition. The thermal cycle at the near-HAZ of the multi-layer deposition was extracted to understand the microstructure evolution (Fig. 10(c)). The near-HAZ underwent three thermal cycles with the peak temperature above the β transus temperature, which caused the dissolution and formation of α phases. Meanwhile, the Subsequent multiple thermal cycles kept the

deposits in the temperature range of 600–977°C for a long time, which promotes the transform of β phases to α phase. Therefore, the metastable β phases translated to acicular α phases due to repeated rapid heating and cooling thermal cycling.

Conclusions

In this work, the finite element model of repairing the blade based on the arc heat source was established to investigate the effect of thermal cycles on the grain and microstructure evolution. The following conclusions can be drawn from this work:

1. Compared to the thermal cycle of direct current arc, the thermal cycle of pulsed arc has an obvious inflection point, which was caused by the thermal undercooling effect of pulsed arc. Meanwhile, the maximum effect of thermal undercooling appears when the peak current transforms to the base current, which will promote the grain refinement.
2. The microstructure of heat affected bands (HABands) is the lamellar microstructure with partial α phase coarsening, which is caused by the longest dwell time of thermal cycle at the temperature range of α phase growth.
3. Compared to the metastable β phases in the near-heat affected zone (near-HAZ) of sing-layer deposition, the microstructure in the near-HAZ of multi-layer deposition becomes extremely fine α phases, which was caused by the repeated thermal cycles.

Declarations

Ethical Approval

Not applicable

Consent to participate

Not applicable

Consent to Publish

Not applicable

Authors Contributions

Yimin Zhuo: Experiment, Methodology, Writing- Original draft preparation **Chunli Yang:** Supervision, Validation. **Chenglei Fan:** Writing- Reviewing, Investigation, Data curation. **Sanbao Lin:** Writing- Reviewing, Validation.

Funding

The National Science and Technology Major Project of China (Grant 2019-VII-0004-0144)

Competing Interests

No conflict of interest exists in the submission of this manuscript, and the manuscript is approved by all authors for publication.

Availability of data and materials

Not applicable

Code availability

Not applicable

Acknowledgments

This work was supported by The National Science and Technology Major Project of China (Grant 2019-VII-0004-0144).

References

1. Srinivasan D. Challenges in Qualifying Additive Manufacturing for Turbine Components: A Review. *Trans Indian Inst Met.* 2021.
2. Denkena B, Boess V, Nespore D, et al. Engine blade regeneration: a literature review on common technologies in terms of machining. *Int J Adv Manuf Technol.* 2015;81:917–924.
3. Zhao H, Zhang G, Yin Z, et al. Three-dimensional finite element analysis of thermal stress in single-pass multi-layer weld-based rapid prototyping. *J Mater Process Technol.* 2012;212:276-285.
4. Sun C, Wang Y, McMurtrey MD, et al. Additive manufacturing for energy: A review. *Appl Energy.* 2021;282.
5. Shan JG, Ren JL, Khorunov VF. Repairing of the defects of the engine vanes of an aeroplane by light beam brazing. *J Mater Process Technol.* 2002;121.
6. Laux B, Piegert S, Rösler J. Advanced braze alloys for fast epitaxial high-temperature brazing of single-crystalline nickel-base superalloys. *J Eng Gas Turbines Power.* 2010; 789-797.
7. Arhami F, Mirsalehi SE, Sadeghian A, et al. The joint properties of a high-chromium Ni-based superalloy made by diffusion brazing: Microstructural evolution, corrosion resistance and mechanical behavior. *J Manuf Process.* 2019;37: 203-211.
8. Huang X, Miglietti W. Wide gap braze repair of gas turbine blades and vanes-a review. *J. Eng. Gas Turbines Power.* 2012(010801).
9. Ye Y, Zou G, Long W, et al. Diffusion brazing repair of IN738 superalloy with crack-like defect: microstructure and tensile properties at high temperatures. *Sci Technol Weld Join.* 2019;24: 1-11.

10. Ma TJ, Li WY, Zhong B, et al. Effect of post-weld heat treatment on microstructure and property of linear friction welded Ti17 titanium alloy joint. *Sci Technol Weld Join*. 2012;17: 180-185.
11. Ma TJ, Chen X, Li WY, et al. Microstructure and mechanical property of linear friction welded nickel-based superalloy joint. *Mater Des*. 2016;89.
12. Parikh VK, Badgajar AD, Ghetiya ND. Joining of metal matrix composites using friction stir welding: a review. *Mater. Manuf. Process*. 2019.
13. Zhang Q, Chen J, Tan H, et al. Microstructure evolution and mechanical properties of laser additive manufactured Ti-5Al-2Sn-2Zr-4Mo-4Cr alloy. *Trans Nonferrous Met Soc China (English Ed)*. 2016;26: 2058-2066.
14. He B, Tian XJ, Cheng X, et al. Effect of weld repair on microstructure and mechanical properties of laser additive manufactured Ti-55511 alloy. *Mater Des*. 2017;119: 437-445.
15. Zhao Z, Chen J, Zhang Q, et al. Microstructure and mechanical properties of laser additive repaired Ti17 titanium alloy. *Trans Nonferrous Met Soc China (English Ed)*. 2017;27: 2613-2621.
16. Zhang J, Yang Y, Cao S, et al. Fine equiaxed β grains and superior tensile property in Ti-6Al-4V alloy deposited by coaxial electron beam wire feeding additive manufacturing. *Acta Metall Sin (English Lett)*. 2020;33.
17. Wanjara P, Gholipour J, Watanabe E, et al. High Frequency Vibration Fatigue Behavior of Ti6Al4V Fabricated by Wire-Fed Electron Beam Additive Manufacturing Technology. *Adv Mater Sci Eng*. 2020;2020.
18. Wanjara P, Watanabe K, De Formanoir C, et al. Titanium Alloy Repair with Wire-Feed Electron Beam Additive Manufacturing Technology. *Adv Mater Sci Eng*. 2019: 1-23.
19. Cunningham CR, Flynn JM, Shokrani A, et al. Invited review article: Strategies and processes for high quality wire arc additive manufacturing. *Addit. Manuf*. 2018;22:672-686.
20. Xu T, Tang S, Liu C, et al. Obtaining large-size pyramidal lattice cell structures by pulse wire arc additive manufacturing. *Mater Des*. 2020;187:108401.
21. Wang J, Lin X, Wang J, et al. Grain morphology evolution and texture characterization of wire and arc additive manufactured Ti-6Al-4V. *J Alloys Compd*. 2018;768 :97-113.
22. Zhuo Y, Yang C, Fan C, et al. Microstructure and mechanical properties of wire arc additive repairing Ti-6.5Al-2Sn-2Zr-4Mo-4Cr titanium alloy. *Mater Sci Technol (United Kingdom)*. 2020;36.
23. Zhuo Y, Yang C, Fan C, et al. Grain refinement of wire arc additive manufactured titanium alloy by the combined method of boron addition and low frequency pulse arc. *Mater Sci Eng A*. 2021;805.
24. Shan XY, Tan MJ, O'Dowd NP. Developing a realistic FE analysis method for the welding of a NET single-bead-on-plate test specimen. *J Mater Process Technol*. 2007;192-193.
25. Goldak J, Chakravarti A, Bibby M. A new finite element model for welding heat sources. *Metall Trans B*. 1984;15.
26. Ding J, Colegrove P, Mehnen J, et al. Thermo-mechanical analysis of Wire and Arc Additive Layer Manufacturing process on large multi-layer parts. *Comput Mater Sci*. 2011;50.

27. Galarraga H, Lados DA, Dehoff RR, et al. Effects of the microstructure and porosity on properties of Ti-6Al-4V ELI alloy fabricated by electron beam melting (EBM). *Addit Manuf.* 2016;10: 47-57.
28. Bambach M, Sizova I, Sydow B, et al. Hybrid manufacturing of components from Ti-6Al-4V by metal forming and wire-arc additive manufacturing. *J Mater Process Technol.* 2020;282: 116689.
29. Zhou Y, Qin G, Li L, et al. Formability, microstructure and mechanical properties of Ti-6Al-4V deposited by wire and arc additive manufacturing with different deposition paths. *Mater Sci Eng A.* 2020;772.
30. Liu Q, Wang Y, Zheng H, et al. TC17 titanium alloy laser melting deposition repair process and properties. *Opt Laser Technol.* 2016;82: 1-9.

Figures

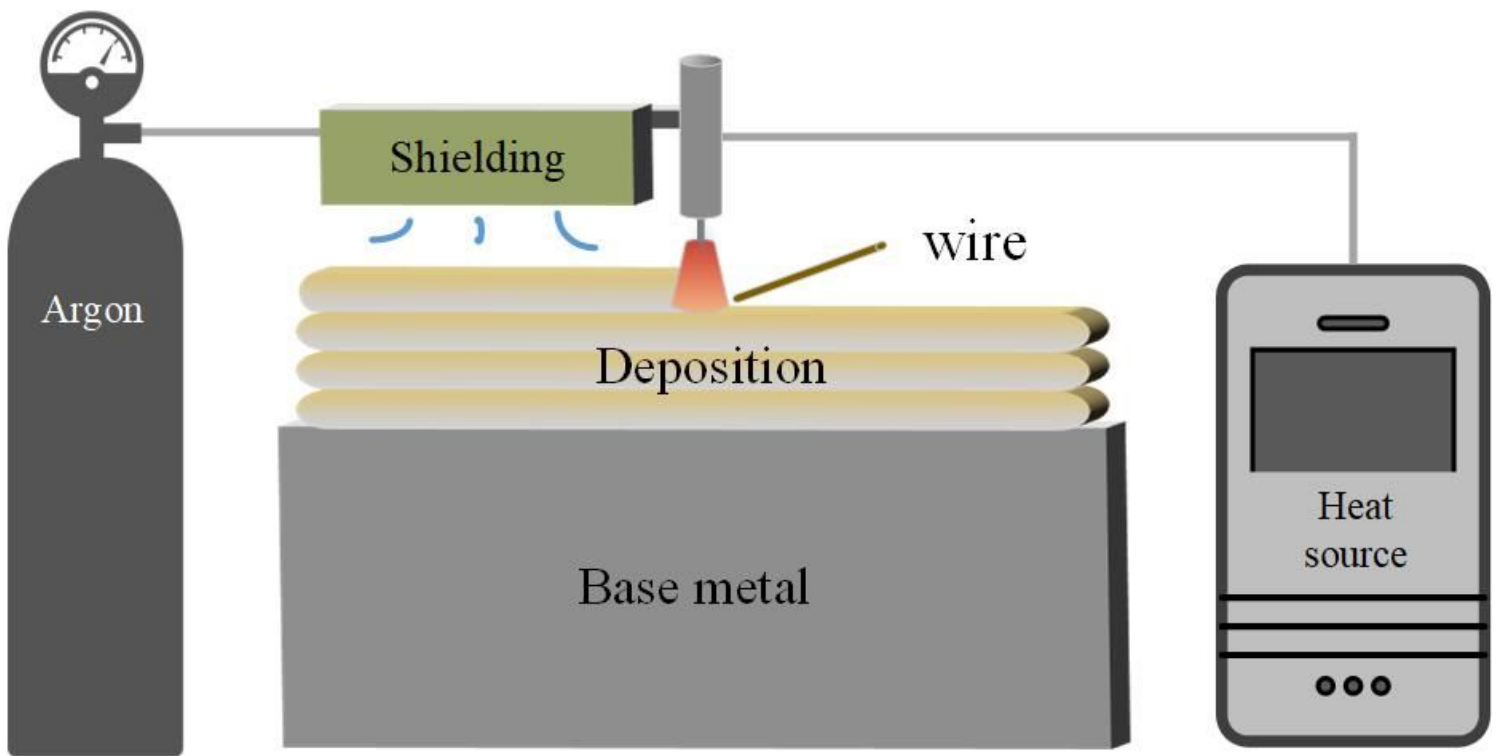


Figure 1

The schematic diagram of repairing titanium alloy by wire arc additive manufacturing.

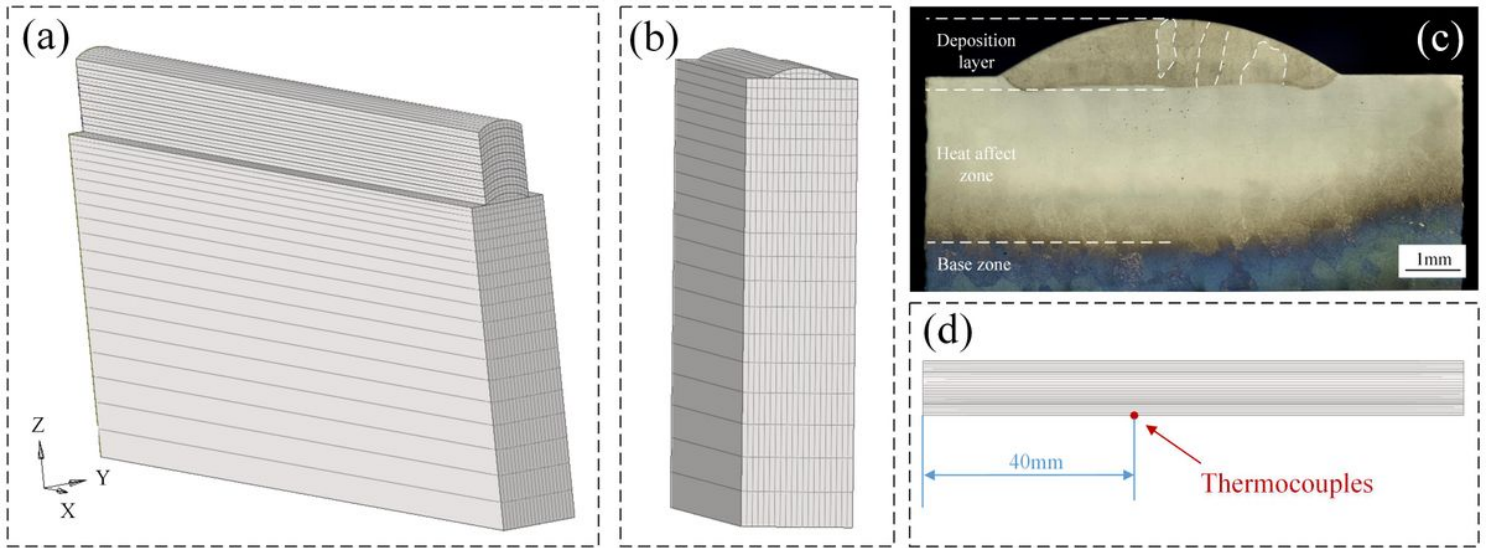


Figure 2

The finite element model and the actual deposition: (a) the mesh model of multi-layer deposition, (b) the mesh model of sing-layer deposition, (c) the cross-section of sing-layer deposition, (d) the measured positions of thermocouples.

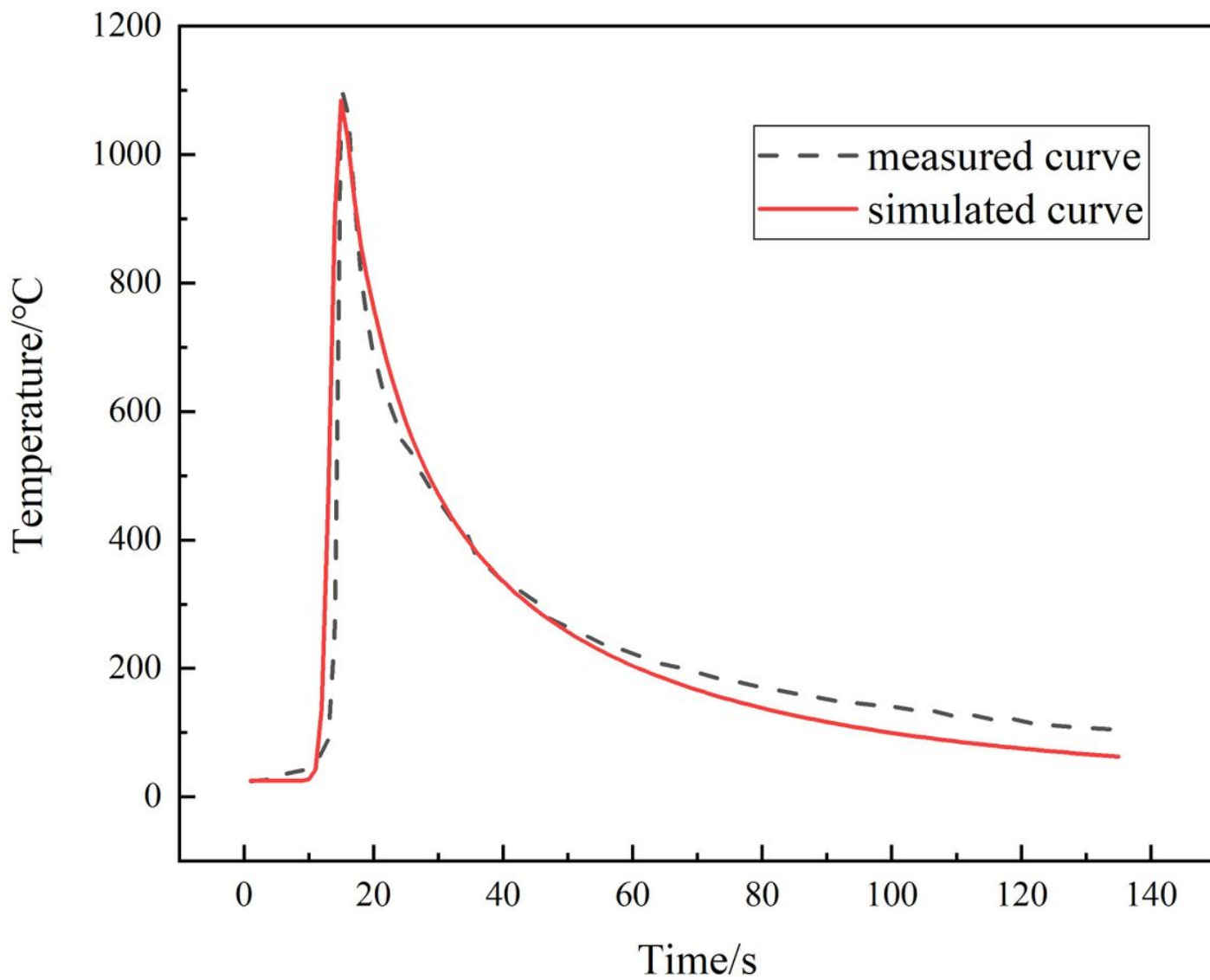


Figure 3

The thermal cycle of the measured and simulated curve.

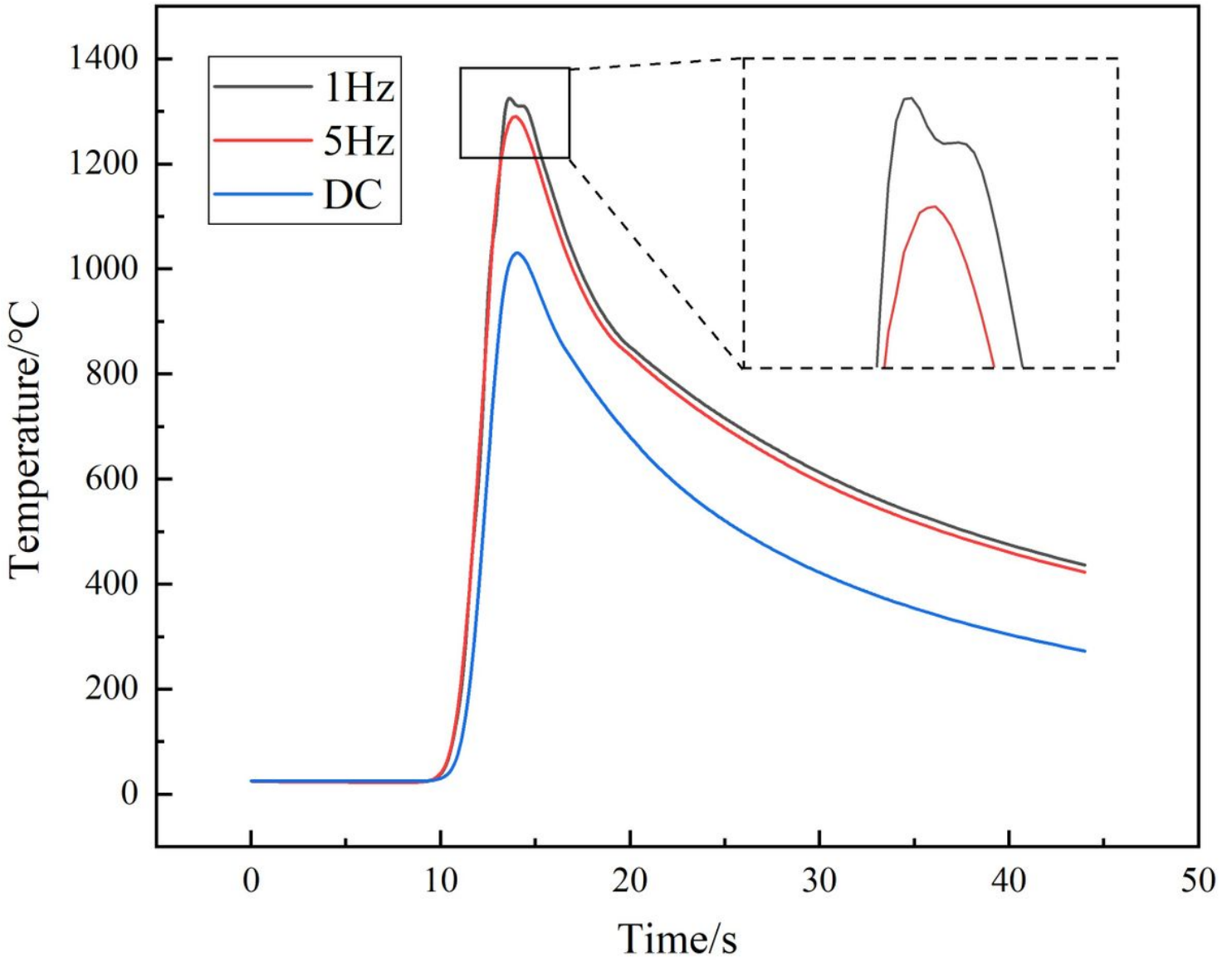


Figure 4

The thermal cycle of different arc types at the measured point.

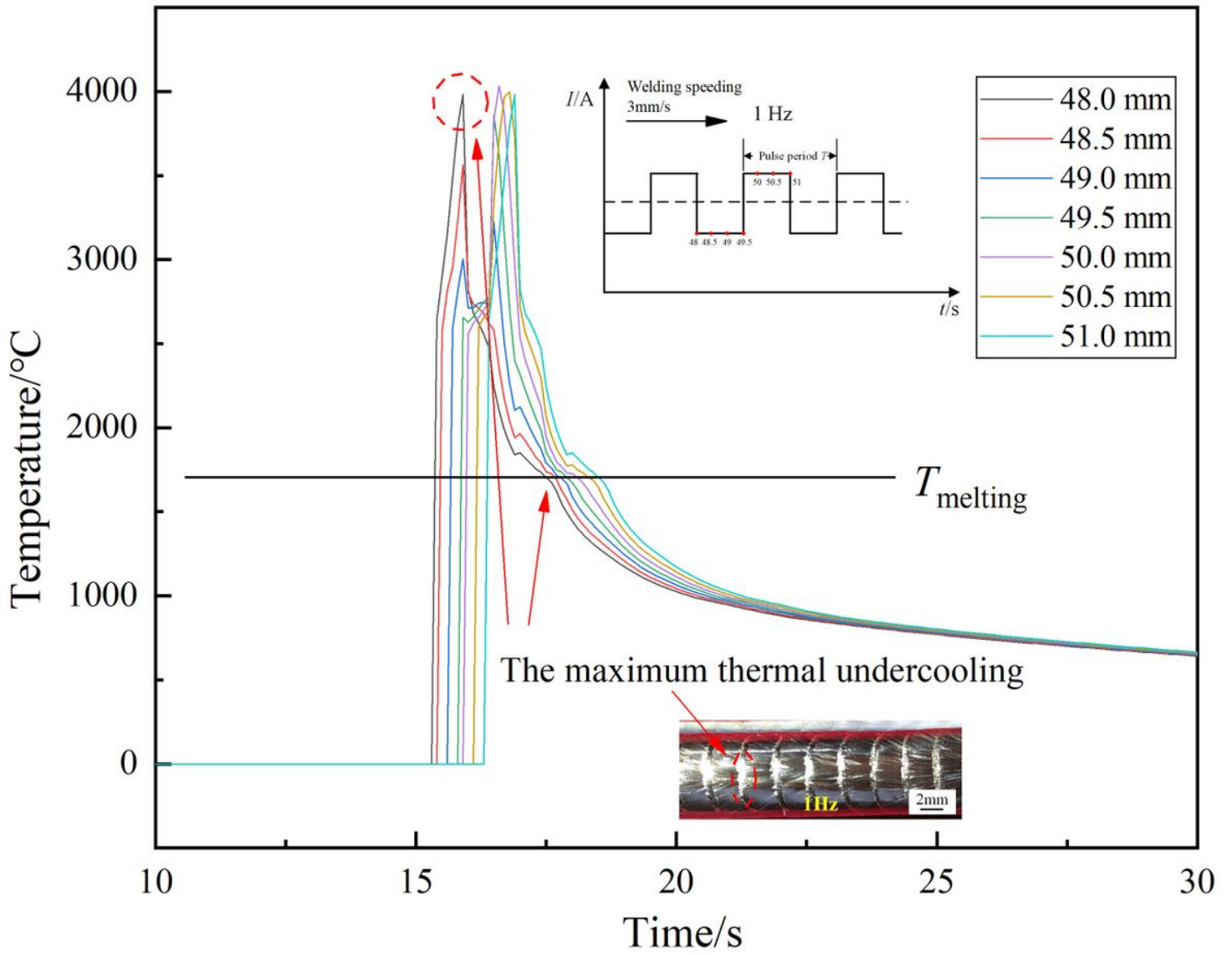


Figure 5

The thermal cycles at different positions fabricated by the 1 Hz pulsed arc, and the corresponding grain morphology (modified by our previous work [23]).

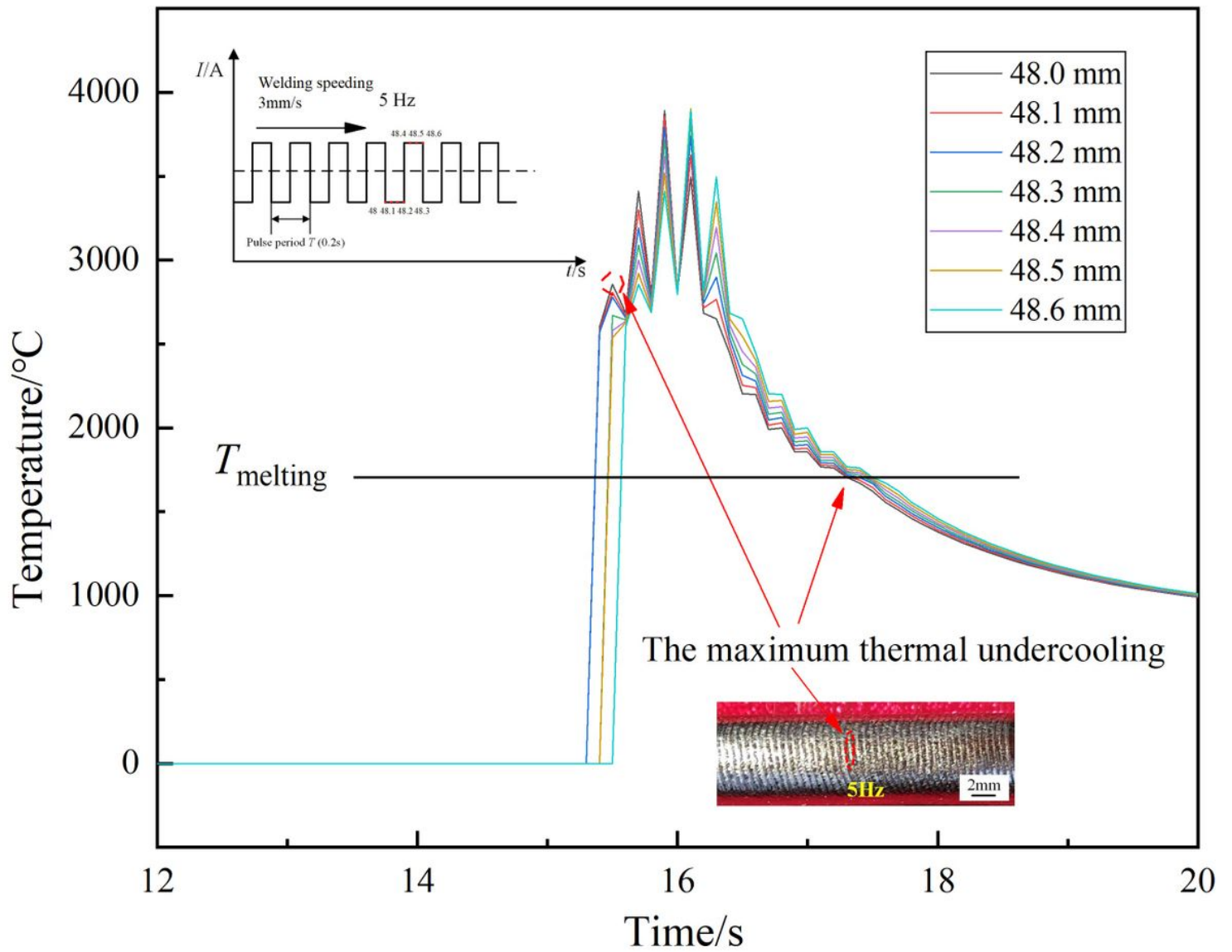


Figure 6

The thermal cycles at different positions fabricated by the 5Hz pulsed arc, and the corresponding grain morphology (modified by our previous work [23]).

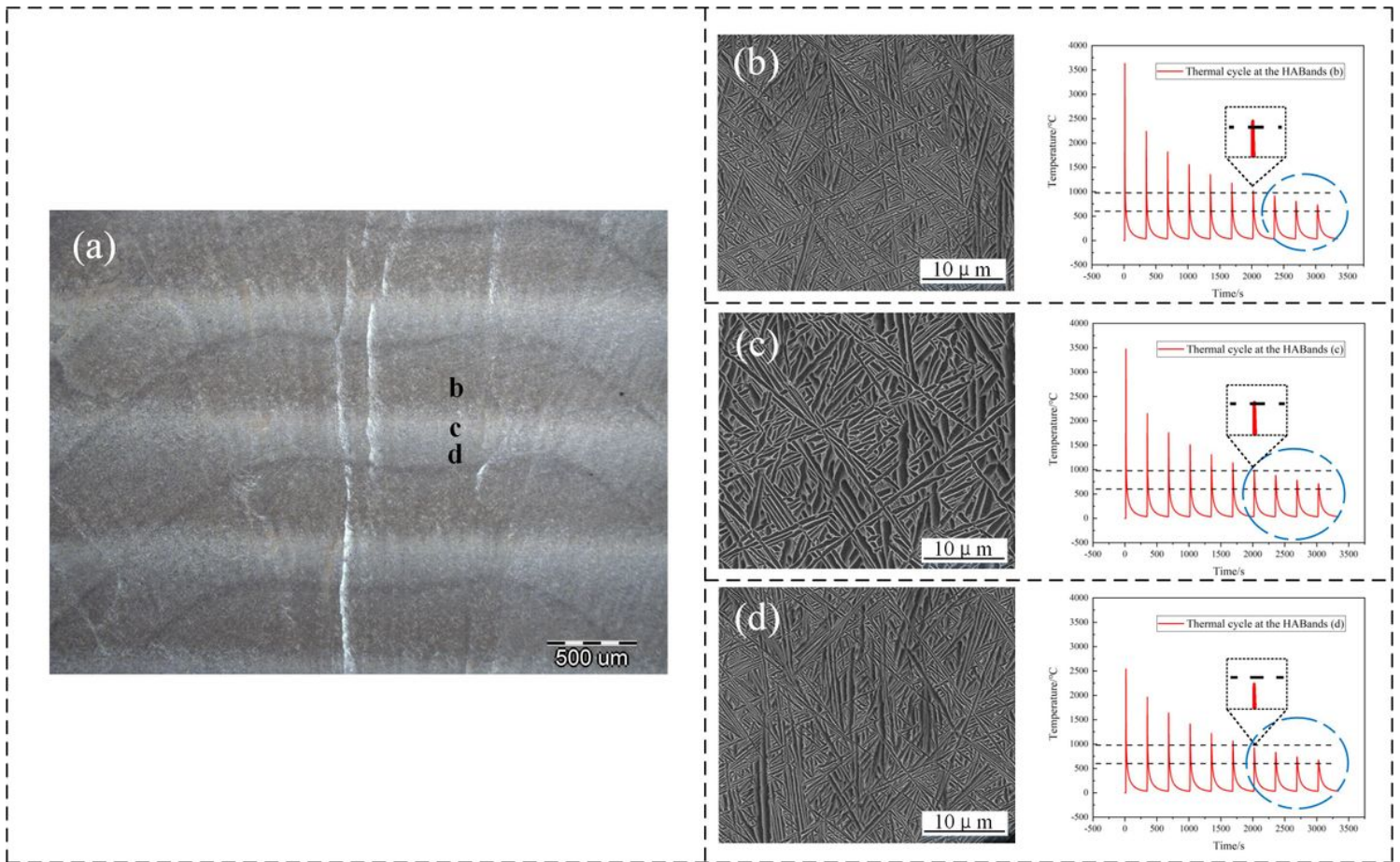


Figure 7

The microstructure and corresponding thermal cycle at the heat affected zone.

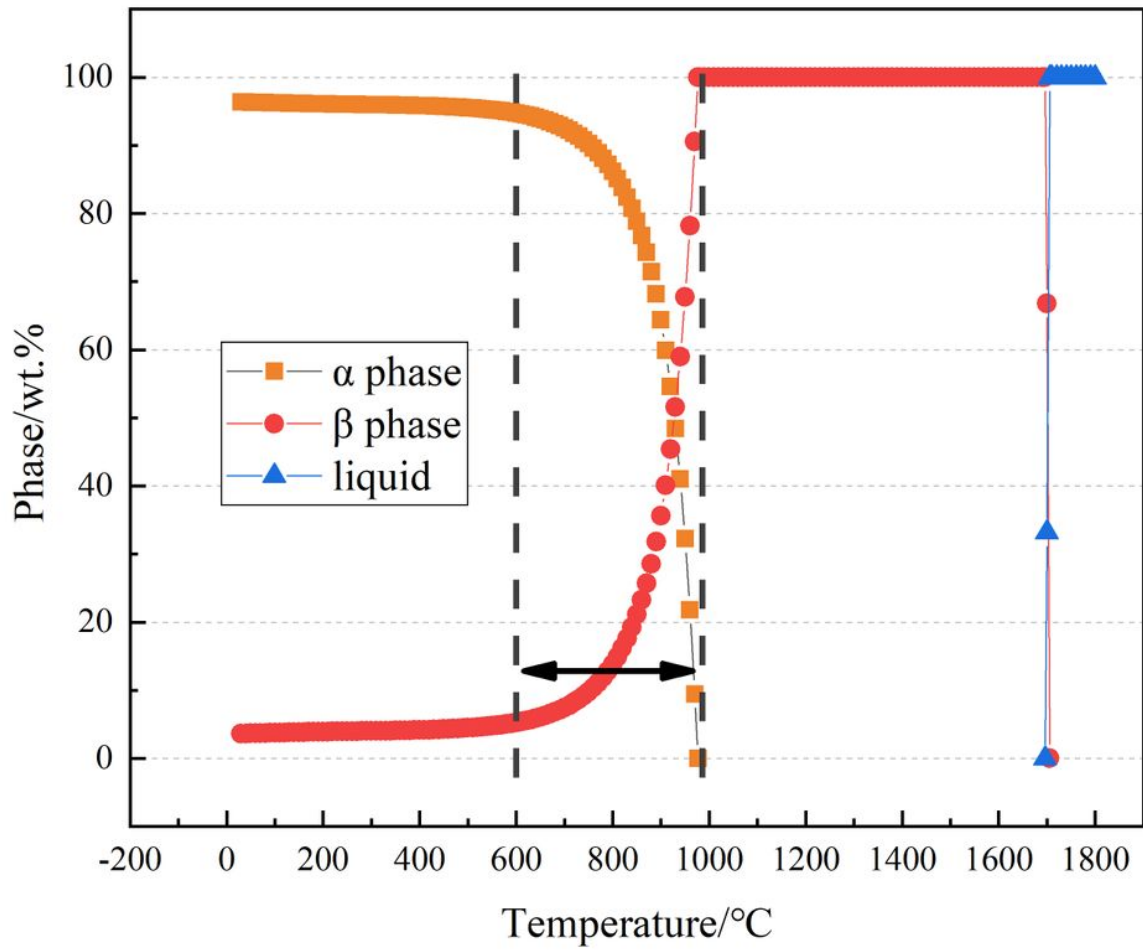


Figure 8

The phase content of TC11 titanium alloy at different temperature.

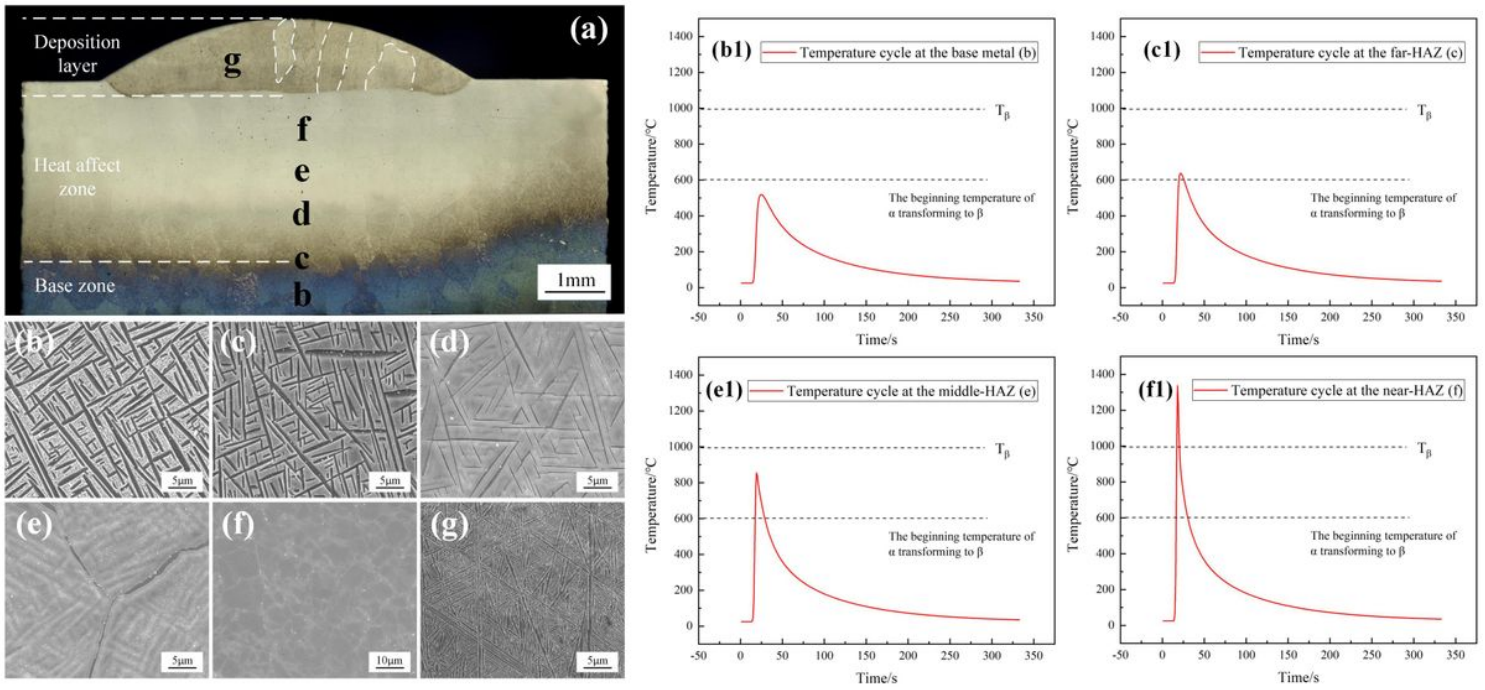


Figure 9

The macrostructure, microstructure and corresponding thermal cycles of the sing-layer deposition: (a) cross section morphology, (b) base metal, (c) far-heat affected zone (HAZ), (d,e) middle- HAZ, (f) near-heat affected zone, (g) the deposition layer.

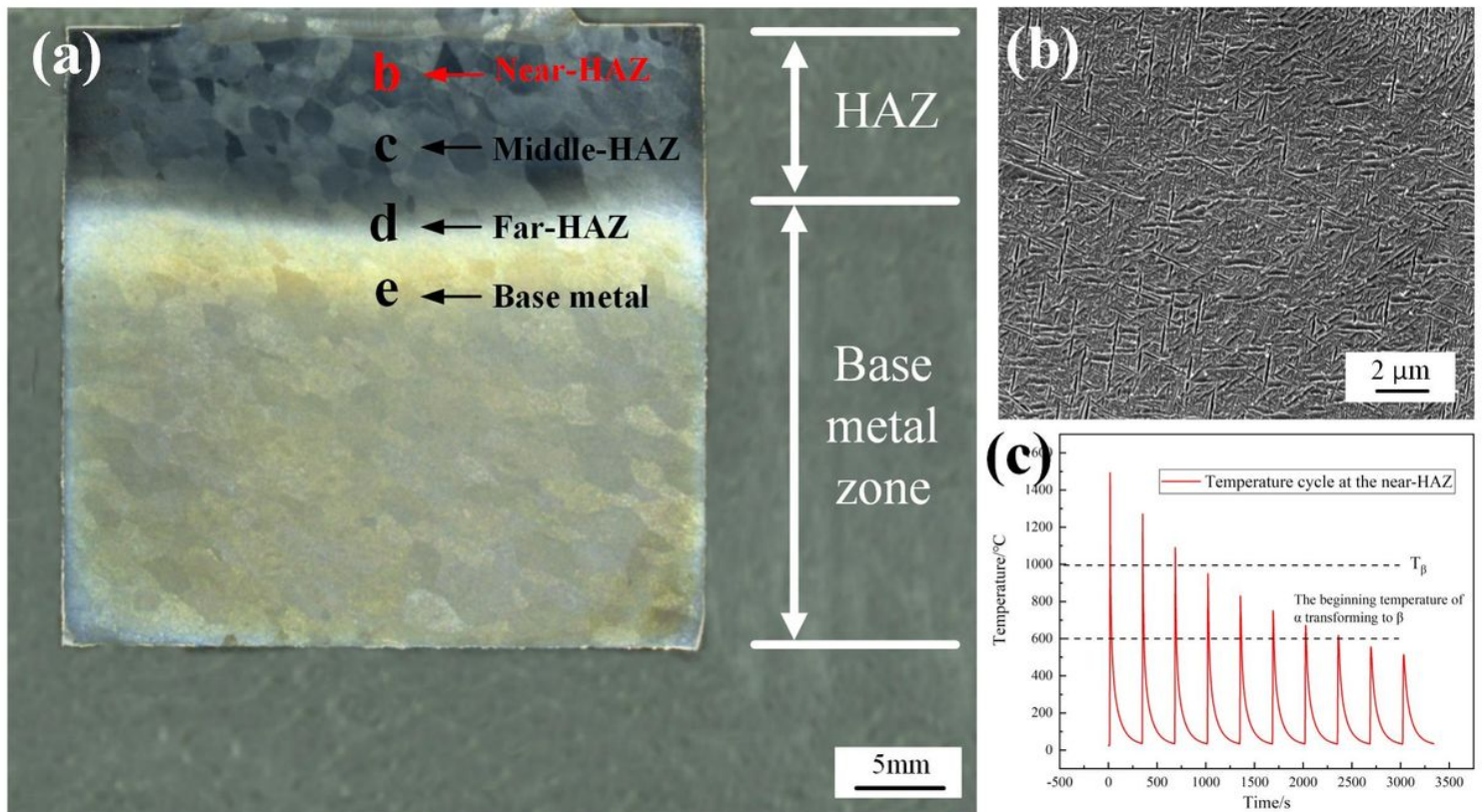


Figure 10

The heat affected zone (HAZ) morphology and corresponding microstructure and thermal cycle: (a) the macrostructure morphology at the HAZ, modified by our previous work [], (b) the microstructure at the near-HAZ, (c) the thermal cycle at the near-HAZ.